J. Fluid Mech. (1988), *vol.* 189, *pp.* 23–51
Printed in Great Britain

Vorticity generation by shock propagation through bubbles in a gas

By J. M. PICONE AND J. P. BORIS

Laboratory for Computational Physics, US Naval Research Laboratory, Washington, DC 20375, USA

(Received 8 September 1986 and in revised form 22 April 1987)

We present a new theoretical model of 'late-time' phenomena related to the interaction of a planar shock with a local, discrete inhomogeneity in an ambient gas. The term 'late-time' applies to the evolution of the inhomogeneity and the flow field after interaction with the incident shock has ceased. Observations of a shock propagating through a bubble or a spherical flame have exhibited or implied the formation of vortex structures and have showed continual distortion of the bubble or flame. Our theory shows that this is due to the generation of long-lived vorticity at the edge of the discrete inhomogeneity. The vorticity interacts with itself through the medium of the fluid, and, depending on the geometry of the discrete inhomogeneity, can roll up into vortex filaments or vortex rings. To verify and amplify this theoretical description, we use numerical solutions of the fluid equations for conservation of mass, momentum, and energy to study the interaction of a weak shock with a cylindrical or spherical bubble. The simulated bubble has either a higher or lower density than the ambient gas. In this way, the calculations provide insights into the effects of both geometry and distortion of the local sound speed. The Mach number of the shock is 1.2, the ambient gas is air, and the pressure is 1 atmosphere. Because of the simple geometry of each bubble, the vorticity generated at the boundary rolls up into a vortex filament pair (cylindrical bubble) or a vortex ring (spherical bubble). The structural features and timescales of the phenomena observed in the calculations agree closely with recent experiments of Haas & Sturtevant, in which helium and Freon bubbles were used to provide the local departures from ambient density. The discussion of results includes a survey of alternative numerical methods, sources of uncertainty in velocities of interfaces or structures, as derived from the laboratory and numerical experiments, and the relationship of our analysis to other theories.

1. Introduction

The propagation of a shock through a non-uniform gas results in refraction, diffraction, and reflection of the shock wave at inhomogeneities that are present. Such deviations from global symmetry distort the transmission of the shock through the gas. In addition, the interactions of pressure waves with density fluctuations in a fluid are a major source of vorticity and turbulent motion (Picone & Boris 1983). These rotational flows evolve on much longer timescales than that of shock passage through the local non-uniformity and can have important long-term effects on the structure and properties of the fluid. Vorticity generation by this and closely related mechanisms (Picone & Boris, 1983) has proven to be significant in studies of the operation of ramjet engines (e.g. see Rudinger 1958), the efficiency of inertial confinement fusion (Emery *et al.* 1984), and the rate at which lightning channels cool (Picone *et al.* 1981).

Shock-tube experiments have been the major source of data on the generation of rotational motion by the interaction of shocks with inhomogeneous gases. Particularly noteworthy are the studies of shock propagation through flames by Markstein (e.g. 1957*a, b*) and the recent work of Haas (1983, 1984) and Haas & Sturtevant (1987) on shock–bubble interactions. Haas & Sturtevant investigated cases in which either single or multiple scatterers (bubbles) were present. Our primary interest is in the spherical-flame and single-bubble experiments of the respective authors. These are, in effect, limiting cases of a fluid in which deviations from ambient are localized and widely separated relative to their representative spatial scales.

Because non-reactive gases were used, the experiments of Haas & Sturtevant provide a good basis for studying vorticity generation by shock interactions with discrete inhomogeneities in a fluid. Haas & Sturtevant used air as the ambient gas, and the bubble contained a mixture of air with either helium or Freon-22. They studied geometrical effects by using bubbles that were cylindrical or spherical in shape. Both Markstein and Hass & Sturtevant noted the appearance of a vortex ring in the axisymmetric geometry (spherical flame or bubble, respectively), but the presence of vortex structures was initially more difficult to discern in shadowgraphs of the cylindrical-bubble experiments (Haas 1983). Markstein (1957*a, b*), Haas (1984) and Haas & Sturtevant (1987) considered linearized impulsive Rayleigh–Taylor instability theory (Richtmyer 1960) in analysing the behaviour of the non-uniformity (the flame or bubble) after passage of the shock. In addition, Haas & Sturtevant used more sophisticated models attributed to Rudinger & Somers (1960) and Taylor (1953), on the one hand, and to Kulkarny (see Haas & Sturtevant 1987, p. 72), Maxworthy (1977), and Didden (1979) on the other. The latter model originally treated vortex generation by impulsive motion of a piston that ejected fluid from the mouth of a short cylindrical chamber.

Recently Picone & Boris (1983) developed a nonlinear theory of shock-generated vorticity. Later Picone *et al.* (1985) applied the theory to the experiments of Markstein, in which a planar shock interacted with a spherical flame. The accompanying numerical simulations of the shock–flame interaction assumed a smoothly varying radial density distribution (Bennett profile) for the flame,

$$\rho(r) = \rho_\infty + \frac{\rho_0 - \rho_\infty}{[1+(r/S_0)^2]^2}.$$

Here ρ_∞ is the ambient density; ρ_0 is the density at the centre of the flame; r is the distance from the centre of the flame; and S_0 is the radius of the flame boundary. The Bennett distribution constrasts with the steep gradient that would be expected at the edge of a flame or a bubble. However, the timescales and velocities in the simulations agreed closely with the experimental values. Both the theory and the simulations showed that the evolution of the system is inherently nonlinear from the time at which the interaction begins.

This work by Picone *et al.* appeared at a highly specialized conference and the work is not well known to the fluid dynamics community. Elements of the theory have begun to appear in the literature (Haas & Sturtevant 1987) through private communications from the present authors. Understanding of the new theory by other authors, however, is far from sufficient to apply it to other relevant problems. The main purpose of this paper is to outline the theory for the fluid dynamics community at large, and to present a numerical and theoretical treatment appropriate to inhomogeneities with sharp, well-defined boundaries.

To reveal the detailed physics of the vorticity-generation process, later sections present numerical simulations of four idealized cases. The cases correspond closely to the experiments of Haas & Sturtevant, including a cylindrical or spherical bubble which is less dense or more dense than the ambient gas (air). Section 3 describes our numerical algorithms and the model based on the numerical algorithms. The Appendix compares our basic numerical algorithms to other potentially useful algorithms with regard to accuracy and the state of the art for modelling the phenomena considered here. Section 4 presents the results of our simulations and compares them with the observations of Haas & Sturtevant. For completeness, this discussion includes comparisons of velocities of interfaces or structures, as derived from the experiments and our numerical simulations. A final subsection analyses the measurement inaccuracies inherent in values reported for these velocities for both the laboratory experiments and the present numerical simulations. In some instances, the same uncertainties are present in both laboratory and numerical experiments. Section 5 summarizes the work and our conclusions.

2. Theoretical analysis

The basis for our theory is the equation

$$\frac{d\boldsymbol{\omega}}{dt}+\boldsymbol{\omega}\nabla\cdot\boldsymbol{v}=\boldsymbol{\omega}\cdot\nabla\boldsymbol{v}+\frac{\nabla\rho\times\nabla P}{\rho^2} \tag{1}$$

which governs the evolution of vorticity $\boldsymbol{\omega}$ in an inviscid fluid. Here the fluid velocity is $\boldsymbol{v}$; the pressure is P; and the mass density is ρ. As shown by (1), misalignment of the local pressure and density gradients leads to a non-zero source term

$$\boldsymbol{S}\equiv\frac{\nabla\rho\times\nabla P}{\rho^2} \tag{2}$$

for the generation of vorticity.

First let us describe the physical process under consideration: a planar shock propagating through a gas and striking a bubble with a circular cross-section. Assume that the bubble has a uniform density which differs from the ambient density. This interaction will result in a shock that is transmitted through the interior of the bubble while a portion of the incident shock diffracts around the edge of the bubble. Because of the curved surface of the bubble, different parts of the incident planar shock will reach the bubble at different times, so the 'refracted' (interior) shock will be curved. In addition, given that the bubble density differs from the ambient gas density, the interior shock will travel at a different speed than the exterior diffracted shock. Ray tracing and geometric acoustics can provide a useful picture of the qualitative features of this process (see Haas & Sturtevant 1987). Section 4 describes our numerical simulations of this process and provides density contour diagrams that follow the evolution of the system.

Now define the x-axis to be a line which is parallel to the direction of propagation of the incident shock and which passes through the centre of the circular cross-section of the bubble. When the incident shock reaches the bubble, the pressure gradient of the shock and the density gradient of the bubble *at the point of contact* will coincide with the x-axis. Equations (1) and (2) tell us that little or no vorticity will be generated under these conditions. As the interaction progresses, however, both the incident (diffracted) shock and the interior refracted shock will have pressure gradients that are not aligned with the density gradient of the bubble, the latter being radially outward from the centre of the bubble. Under these conditions, the vorticity source term in (2) is non-negligible, and significant vorticity is generated at the edge of the bubble, where the density gradient is non-zero. As the diffracted and refracted shocks reach the downstream side of the bubble, the pressure gradients of the shocks and the bubble density gradient will again be approximately aligned and the source term will again be small where the bubble intersects the x-axis. The vorticity plots in §4 follow the evolution of this process.

The vorticity vector will be perpendicular to the plane defined by the circular cross-section of the bubble. Notice that, in this plane, the sign of the vorticity generated along the edge of the bubble will be opposite on opposite sides of the x-axis. The rotational motion induced by the non-zero vorticity distorts both the bubble and the vorticity distribution itself. The latter rolls up into vortex structures (a pair of vortex filaments or a vortex ring) appropriate to the underlying symmetry of the bubble (cylindrical or spherical, respectively).

2.1. *Vortex strength*

Continue to define the x-axis as above. For a system that varies only in the (x, y)-plane, the vortex strength in the region $(y \geqslant 0)$ containing the upper half of the bubble is the solution to the following equation:

$$\frac{\mathrm{d}\kappa}{\mathrm{d}t} = \int_{A(t)} \frac{\nabla\rho \times \nabla P}{\rho^2} \mathrm{d}A(t), \tag{3}$$

which we obtain by integrating (1) in a Lagrangian sense over the area $A(t)$ containing the upper half of the bubble and moving with the bubble. Performing the integral over the time of passage of the shock through the bubble (Picone *et al.* 1985) gives the following relation for the magnitude of the vortex strength or circulation κ:

$$\kappa \approx 2V_2\left(1-\frac{V_2}{2W}\right)S_0 \ln\left(\frac{\rho_\infty}{\rho_b}\right). \tag{4}$$

Here V_2 is the flow velocity behind the shock in the laboratory frame, W is the shock velocity, S_0 is the radius of the cross-section of the bubble, ρ_∞ is the ambient density, and ρ_b is the density of the gas in the bubble. To perform the integration, we assumed the shock to be a planar discontinuity, ignoring the effects of curvature and differences between strengths of the (interior) refracted shock and (exterior) incident and diffracted shocks. The detailed evolution of the system revealed by the numerical simulations (§4), when combined with the theory, (2), indicates that the distortion and interaction of the various shocks will lead to a reduction in vortex strength relative to that given by (4). Measurements of the vortex strength from the simulation data confirm that prediction. However, scaling arguments (Picone & Boris 1983) indicate that the functional variations and trends (for example, with V_2 and shock velocity W) in (4) are correct.

The fact that (4) provides accurate scaling relationships among the various parameters in the problem is of great use in understanding both the laboratory experiments and the numerical simulations. An example of the former occurs in analysing the speed at which the vortex structures and the bubble propagate sometime after interaction with the shock has ceased. The propagation velocities of a vortex filament pair or a vortex ring are proportional to the vortex strength κ.

Equation (4) shows that the velocities, when normalized by V_2 (the flow speed behind the incident shock) will decrease with increasing Mach number, since V_2/W will increase with Mach number. Experiment has verified this prediction (Haas & Sturtevant 1987). Other theories have been unable to verifiy this result (see discussion in Haas & Sturtevant 1987). Section 4 shows how (4) can aid in the analysis of numerical simulations as well.

2.2. *Relationship to Rayleigh–Taylor instability*

The conventional Rayleigh–Taylor instability theory begins with an infinitesimal spatial perturbation which exists for a long (infinite) period of time relative to the growth rate of the perturbation. A previous paper (Picone *et al.* 1985) pointed out that the source term of the vorticity evolution equation, (2), provides the generalization of the usual notion of Rayleigh–Taylor instability to the entire conceivable range of space scales, timescales, and perturbation geometry. In particular the problem considered in this paper consists of a finite 'perturbation' (the bubble) and a finite timescale over which vorticity is produced (the time for shock passage through the bubble). The bubble introduces another difference from the usual picture, since the perturbation is not sinusoidal. This is a fundamental departure from the impulsive Rayleigh–Taylor or Richtmyer–Meshkov (Richtmyer 1960; Meshkow 1970) instability, in which a planar shock passes through a rippled interface or a perturbed shock passes through a planar interface. Such a system can initially show linear growth. In constrast, the shock–bubble interaction with the subsequent flow-field evolution represents a nonlinear process from the beginning, as discussed above. Arguments have been made that the linear theory can fit the shock–bubble problem by treating the side of the bubble facing the shock as part of a sinusoidal density discontinuity of wavelength $2\pi R (R = \text{bubble radius})$. However, as shown by the calculations in §4 and the laboratory experiments (Haas & Sturtevant, 1987), the subsequent distortion of the upstream edge of the bubble by the vorticity field has an apparent wavelength of about $\frac{4}{3}R$. The choice of wavelength for the linear theory is therefore ambiguous. In spite of this ambiguity, the linear theory has provided valuable insights (Markstein 1957*a*, *b*; Haas & Sturtevant 1987). Haas & Sturtevant (1987) have discussed the relationship between linear theory and experiment in detail and have provided an excellent picture of the strengths and limitations of the linear theory.

2.3. *Other theories of vortex formation*

Haas & Sturtevant have discussed two additional models of vortex formation and have related them to the experiments which have been simulated here. The first, due to Rudinger & Somers (1960), describes the process as an acceleration of the bubble during the initial transients and transformation into a vortex ring in analogy to Taylor's (1953) 'dissolved' vortex-generating disk. The second was an adaptation by Haas & Sturtevant of models developed by Kulkarny (see Haas & Sturtevant 1987, p. 72), Maxworthy (1977), and Didden (1979) for vortex-ring formation by impulsive fluid flow from the mouth of a tube. The application of those ideas by Haas & Sturtevant treated the air jet observed in the two helium cases as a piston which generates vorticity. Given the dynamics of vorticity generation demonstrated by our simulations, neither mechanism adequately describes the actual physical process. The key element here is that vorticity resides on the edge of the bubble from the time by which the incident shock interacts with the bubble. Further, the vorticity interacts with the surrounding fluid to produce a jet and interacts with itself through the medium of the fluid to produce compact structures – filaments or a ring. Here we use the term 'vortex filament' in the sense of Lamb (1945), to denote the fluid within a vortex tube having a finite cross-section, as opposed to a vortex line. In a two-dimensional (x,y) Cartesian system, a finite vortex represents the cross-section of a vortex filament whose axis is a straight line perpendicular to the (x,y)-plane.

Given the above discussion, impulsively generated motion of the bubble through the ambient gas does not itself produce the observed vorticity and the jet is the symptom rather than the cause of the vorticity generation. In addition, the theory outlined in § 2.1 applies equally to all four cases, whereas the piston-generator theory appears to apply to the helium cases only. Note, however, that these models are still quite useful in providing insights into the observed phenomena.

3. Numerical simulations

We have used the FAST2D computer code (Picone & Boris 1983; Book *et al.* 1981) to simulate the interaction of a planar shock with four types of discrete inhomogeneities (cylindrical, spherical; less dense than ambient, more dense than ambient). Our primary objectives are to investigate the theoretical picture presented in the previous section and to provide a thorough understanding of the basic physical phenomena associated with the generation of vorticity through the shock–bubble interaction. Because the shock tube experiments of Haas & Sturtevant (1987) provide an excellent point of reference, the initial conditions for the numerical simulations match those of Haas & Sturtevant to the extent possible within the limits of the numerical model. The design of the model permits a close comparison of the evolving morphology of the numerically simulated flow field and bubble with structural features observed in the laboratory shadowgraphs. More detailed modelling of the laboratory experiments (i.e. to obtain closer quantitative agreement) was not necessary to reveal the physical processes accompanying vorticity generation.

This section presents the following: (i) the basic numerical algorithm for hydrodynamics in FAST2D, including an assessment of numerical accuracy, and (ii) details of the numerical model for shock–bubble interactions. The Appendix provides a survey of those numerical algorithms for hydrodynamics that have been used to treat at least some of the phenomena encountered in the problem under consideration. To be adequate for our purposes, however, an algorithm must be applicable to *all* of the phenomena involved. This includes non-steady, supersonic, compressible flows (shocks) which generate non-steady, complex rotational flows embedded in a compressible medium. The Appendix assesses the ability of other algorithms to satisfy this criterion, the cost and complexity of each technique, and the present degree of success in implementing each algorithm in practical computer codes. In this way, the authors hope to provide the reader with some perspective on the methods used in the present simulations. To complete our assessment of the numerical model, the last part of § 4 discusses the relationship between the laboratory and numerical experiments, including measurement uncertainties common to both or unique to either.

3.1. *The FAST2D computer code*

The FAST2D algorithm employs time-step splitting in conjunction with flux-corrected transport (FCT: Boris & Book 1976; Zalesak 1979) to solve the fluid equations for conservation of mass, momentum, and energy for inviscid, compressible flows:

$$\frac{\partial \rho}{\partial t}+\nabla\cdot(\rho v)=0, \tag{5a}$$

$$\frac{\partial \rho v}{\partial t}+\nabla\cdot(\rho v v)=-\nabla P, \tag{5b}$$

$$\frac{\partial E}{\partial t}+\nabla\cdot(E v)=-\nabla\cdot(P v), \tag{5c}$$

where

$$E=\frac{P}{\gamma-1}+\tfrac{1}{2}\rho v^2 \tag{5d}$$

is the total energy density and γ is the ratio of specific heats. The FCT algorithm is state-of-the-art for treating supersonic compressible flows involving discontinuities like shocks. In the region of a discontinuity, FCT uses a time- and space-centred-difference scheme with additional zeroth-order diffusion to integrate the conservation equations. The presence of the diffusion prevents dispersive ripples and instability near discontinuities in the flow field. As the distance from the discontinuity increases, the algorithm then transitions nonlinearly to a second-order scheme that is similar to the Lax–Wendroff algorithm (Richtmyer & Morton 1967). This scheme has fourth-order phase accuracy and fourth-order dissipation. In this way, the numerical method remains stable in the vicinity of a discontinuity while maintaining high-order accuracy in the vast majority of cells where no discontinuity exists. The FCT algorithm does suppress short-wavelength variations (around two cells or less). This paper will be concerned only with large-scale rotational motion, which contains most of the energy and which FCT treats very accurately. The FAST2D code has produced excellent agreement with data from a variety of experiments, including studies of shock reflections from wedges in non-reactive fluids (Book *et al.* 1981) and studies of detonation cell structure, in which the reactive chemistry was modelled (Oran *et al.* 1983). Grinstein, Oran & Boris (1986) have successfully applied FAST2D to subsonic rotational flows.

One especially noteworthy feature of the FAST2D code and the FCT module contained therein is that of adaptive gridding, which maintains the greatest resolution at the smallest features to be studied in the flow. This feature reduces costs significantly by permitting cells of varying size, as long as the variation in dimensions from cell to cell is less than 25%. In addition, various regions of the grid can move with waves or other fluid structures. This is accomplished by comparing the grid cells from time step to time step and computing the velocity U_{gi} of each cell i. The FCT algorithm computes changes in the conserved quantities in terms of the net flux of each quantity (e.g. mass) into the cell, which involves the quantities v_i-U_{gi}, where v_i is the fluid velocity in cell i. Boris (1976) has described this procedure in detail, and rigorous tests of the adaptive-gridding algorithm have been peformed (e.g. Book *et al.* 1981) in especially demanding problems involving strong shocks. We use this feature to provide better resolution of the bubble boundary. The subsonic flows that are present at the bubble deforms and evolves represent no problem for the adaptive-gridding feature.

3.2. *Numerical model*

Figure 1 shows a schematic of the computational domain with the initial conditions inside the domain and the boundary conditions for the calculations. The heavy black

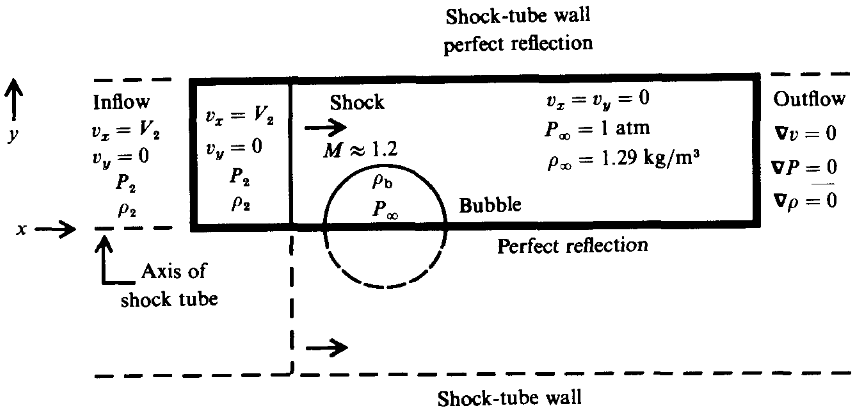

FIGURE 1. Schematic of boundary conditions and initial conditions for the calculations. The heavy black line surrounds the computational domain, which coincides with the upper half of the shock tube, the latter being indicated by dashed lines. See the beginning of § 3.2 for details.

line surrounds the computational domain, with the y-axis vertical and the x-axis horizontal for the cylindrical bubble cases. In the spherical (axisymmetric) cases, the r-axis is vertical and the z-axis is horizontal. The dashed lines show the upper and lower edges and the axis of the shock tube to indicate where the computational domain lies. Not shown explicitly are boundary cells that surround the computational domain and which contain the parameter values necessary to maintain the desired conditions at the edge of the computational domain.

The upper boundary of the grid coincides with the upper edge of the shock-tube wall. Because the upper half of the system is a mirror image of the lower half, the calculations include only the upper half, as shown. The lower boundary of the grid thus coincides with the shock-tube axis. Both the upper and lower boundaries of the computational grid are treated as perfectly reflecting. The incident shock moves from left to right in figure 1. Throughout the calculation, the left boundary cells contain parameter values ($\rho_2, P_2, v_x = V_2, v_y = 0$) corresponding to the region behind a planar shock of Mach number 1.23 (cylindrical-bubble case) or 1.25 (spherical-bubble case). As shown inside the computational domain, the same values are used as initial conditions behind the shock, which lies a few cells inside the computational grid. The left boundary condition also permits smooth outflow of reflected waves produced by the shock–bubble interaction. The right boundary condition must similarly permit the smooth outflow of any rightward-moving waves, including the distorted incident shock. Figure 1 shows that this is accomplished by maintaining a 'zero gradient' in all fluid variables (e.g. $\nabla v = 0$) at the right boundary. Although more sophisticated treatments are available (Grinstein *et al.* 1986), tests have shown our method to be sufficient.

The computer model simulates a two-dimensional cross-section of the cylindrical-bubble cases by using Cartesian coordinates. The x-axis is horizontal and the y-axis is vertical, as shown in figures 2, 3, 6 and 7. The calculation thus corresponds to a planar shock interacting with an infinitely long cylindrical bubble, the axis of which is perpendicular to the shock-tube axis. The shock tube in the experiments was horizontal as in our figures.

Cylindrical coordinates (r, z) are necessary to treat the case of the planar shock interacting with a spherical bubble. As shown in figures 4, 5, 8 and 9, the z-axis coincides with the axis of the shock tube, and the r-axis is vertical. Again the simulation includes only the upper half of the system. Because of the azimuthal symmetry about the z-axis, the semicircle in figure 4 represents a cross-section (great circle) of a sphere. The boundary conditions are the same as those described in the first paragraph. Notice that, in the case of the cylindrical bubble, the calculation treats the shock tube as having an infinite slab geometry with the infinite dimension perpendicular to the computational grid. In the axisymmetric case (spherical bubble), our simulated shock tube is a cylinder.

Besides the existence of both supersonic and long-term rotational flows, this problem contains further computational difficulties involved with the presence of two fluids of different density separated by a discontinuous interface. A curved, discontinuous interface on a rectilinear differencing grid would have a jagged boundary characteristic of the edges of the grid cells. The initialization of a bubble on the rectilinear differencing grid thus requires some care, since the bounding surface might not be as smooth as in the experiment. If the boundary were initially too irregular, the impulsive Rayleigh–Taylor (Markstein 1957*a*, *b*) or Richtmyer–Meshkov instability could be induced by passage of the shock through the surface. In early tests, we initialized the density without regard to this consideration, so that

$$\rho(\boldsymbol{r}_{ij}, t) = \begin{cases} \rho_b, & \text{if } |\boldsymbol{r}_{ij} - \boldsymbol{r}_b| \leqslant S_0, \\ \rho_\infty, & \text{otherwise.} \end{cases}$$

Here $\boldsymbol{r}_{ij}$ labels the position of grid cell (i, j); $\boldsymbol{r}_b$ is the location of the centre of the two-dimensional bubble; ρ_b is the density of the bubble gas; ρ_∞ is the density of the ambient gas; and S_0 is the radius of the bubble. After passage of the shock through the bubble, slow linear growth of a small numerically induced ripple occurred at the downstream edge of the 'light' bubble (density less than ambient) near the shock-tube axis. According to (1) and (2), the shock should generate little vorticity there if the numerical boundary were smooth.

Although this small instability did not intefere with the large-scale flows of interest, the authors have added several features to the code to improve the regularity of the 'numerical' bubble surface and eliminate such phenomena:

(i) The computational grid has an embedded region of fine cells surrounding the bubble. This fine grid moves with the bubble to maintain the necessary resolution of the bubble boundary while minimizing the cost of the calculation (see §3.1). The approximate speed of the bubble thus defines the velocity of the fine grid and can be estimated from the velocity V_2 of fluid behind the incident shock and the vortex strength κ in (4), according to the equation

$$V_b \approx V_2 + \frac{\kappa}{4\pi d}.$$

Here V_b is the velocity of the bubble and d is the perpendicular distance of the vortex core to the axis of the shock tube. The authors stopped the calculation and checked the placement of the grid periodically, adjusting the velocity of the fine grid when necessary. At the edges of the fine grid, the cell dimensions transition smoothly to those of the remaining coarse cells. This smooth transition ensures the numerical stability and accuracy of the FCT algorithm throughout the grid.

(ii) To *initialize* the calculations, the model interpolates carefully between the ambient density and the density of the gas in the bubble for the cells through which the bubble boundary (circle of radius S_0) passes. The interpolation depends on the fraction α_{ij} of boundary cell area that falls inside the bubble radius. In each boundary cell (i, j), the mass density at time $t = 0$ is

$$\rho(\boldsymbol{r}_{ij}, 0) = \alpha_{ij}\rho_b + (1-\alpha_{ij})\rho_\infty.$$

Because this is done before the calculation begins and because FAST2D explicitly conserves mass, momentum, and energy, this interpolation has no effect on the conserved quantities.

(iii) A diffusive smoothing technique spreads the boundary over approximately two cells *before* the calculation begins. This does not degrade the calculation because FCT will not maintain a discontinuity over fewer than two cells (see the Appendix). Again this intialization does not affect conservation.

The thicker smoother boundary at time $t = 0$ eliminates numerically induced Richtmyer–Meshkov instability from the simulations. An alternative approach would have consisted of significantly reducing the sizes of the grid cells. This would have added considerable expense to the calculation *at each time step* by increasing the number of grid cells and by decreasing the time-step size, proportional to the smallest grid-cell dimension. The latter increases the number of time steps covering a given amount of elapsed time. A factor of two decrease in each cell dimension while maintaining the same system size would increase the computer-time expenditure by approximately a factor of eight.

The need to resolve the bubble surface well has led to the use of 100 cells in the fine grid which surrounds the bubble throughout the calculation. The sensitivity of the FAST2D computer code to grid cells size has been the subject of extensive testing (e.g. Grinstein *et al.* 1986). The result has been that, for resolution like that used here, changes of $\pm 50\%$ have made no difference in the observation of evolving large-scale fluid structures and only slight differences in values of the fundamental variables (e.g. mass density, fluid velocities, etc.). Since FAST2D respresents discontinuities as being spread over 2–3 cells, the uncertainty in locating physical interfaces will decrease with decreasing cell size. This affects the quantitative determination of structural velocities from the numerical data. Section 4.6 discusses this and other considerations in interpreting such velocities. The physical description of the phenomena, in which we are primarily interested, however, does not change significantly, and the cost of higher resolution (factor of eight in cost for cell dimensions of half the original size) is not justified.

The model does not account for the effects of surface tension of a physical bubble surface, nor does the code include a physical viscosity. The surface tension is small (Haas 1984); however, it will act to suppress the growth of instability on the surface of the bubble (§4.3). As to viscosity, the FCT algorithm has a large numerical dissipation (effective viscosity for the momentum density) in the vicinity of discontinuities to ensure a well-behaved solution there. By construction, however, this viscosity cannot spread the discontinuities over more than 2–3 cells (see the Appendix). Tests of the FAST2D code with realistic diffusive terms added have shown that, on the timescales of the system evolution, such terms make very little difference, especially for the large-scale phenomena studied here. This is easy to see, since at room temperature the kinematic viscosity, the molecular diffusivity, and the thermal diffusivity are all approximately 0.2 $\mathrm{cm^2/s}$ (Batchelor 1967, p. 594). This would cause very little spreading of fluid structures on timescales of 1 ms or so, as in these simulations.

4. Results of numerical simulations

Our primary interest lies in the mechanisms and phenomenology of vorticity generation and the late time evolution of the system. Thus the discussions and figures below do not deal in detail with the shock diffraction, reflection, and refraction by the bubbles. A larger number of density contours would shed more light on this aspect; however, a future paper examines the very early time phenomena using a new finite-element compressible code (Löhner, Picone & Boris 1988). Haas & Sturtevant (1987) have already explained the major qualitative features of these processes in terms of geometric acoustics.

4.1. '*Light*' *cylindrical bubble*

Figures 2 and 3 show density and vorticity contour diagrams for the interaction of a planar shock of Mach number $M = 1.23$ with a cylindrical bubble that is less dense than the ambient gas ('light' cylindrical bubble). The bubble has a diameter $D = 51$ mm. The vertical dimension of the simulated shock tube is 8.9 cm while the dimension perpendicular to the figure is infinite. In the experiment of Haas & Sturtevant, the test section had a square cross-section of 8.9 cm on a side. The density of the gas inside the bubble is 0.214×10^{-3} g/cm^3, which falls in the middle of the range of densities used by Haas & Sturtevant. The density of the ambient gas is 1.29×10^{-3} g/cm^3 and the pressure is 1 atm. The Cartesian grid consists of 150×50 cells. There are 50×50 coarse cells of dimensions $\Delta x = 0.422$ cm and $\Delta y = 0.089$ cm and 100×50 fine cells of dimension 0.089 cm on a side. The fine cells surround and travel with the bubble. These calculations have used a ratio of specific heats $\gamma = 1.4$ (see §4.6). The initial conditions behind the planar incident shock were $\rho_2 = 1.80 \times 10^{-3}$g/cm^3, $P_2 = 1.62 \times 10^6$ dyn/cm^2 and $V_2 = 1.15 \times 10^4$ cm/s.

The vorticity contour diagrams show that positive vorticity is produced along the upper edge of the bubble, excluding regions near the axis of the shock tube (x-axis) where the pressure gradient of the shock and the density gradient at the edge of the bubble are aligned. This is consistent with the source term in (2). Positive vorticity results because the density gradient is radially outward for a bubble that is lighter than ambient. By symmetry, negative vorticity resides along the lower interface of the bubble with the ambient gas. A comparison with the density contour plots ($t = 44$ μs) shows that the generation of vorticity tracks the progress of the refracted shock that is inside the bubble and that precedes the incident shock. In the case of bubbles that are heavier than ambient ('heavy' bubble case), the vorticity generation seems to track the portion of the incident shock that is outside the bubble and that precedes the refracted shock inside the bubble. Our conclusion is that both shocks actually contribute to the vorticity, which appears to track the shock that travels fastest. The refracted shock in the light-bubble case generates less vorticity over the downstream half of the bubble since the associated pressure gradient is more nearly aligned with the density gradient of the bubble than a planar shock would be. In addition, the (diffracted) incident shock interacts more weakly with the downstream half of the bubble because of intersection with the primary and secondary transmitted waves (Haas & Sturtevant 1987) which arrive first at the downstream side (see figure 2, $t = 129$ μs). The values of the vortex strength computed from the simulations are smaller owing to these factors (§4.5).

The rotational motion associated with the vorticity pulls a jet of ambient gas through the centre of the bubble. As the bubble deforms, the vorticity distribution rolls up with the fluid to form a vortex filament pair (see §2.3 for definition). This

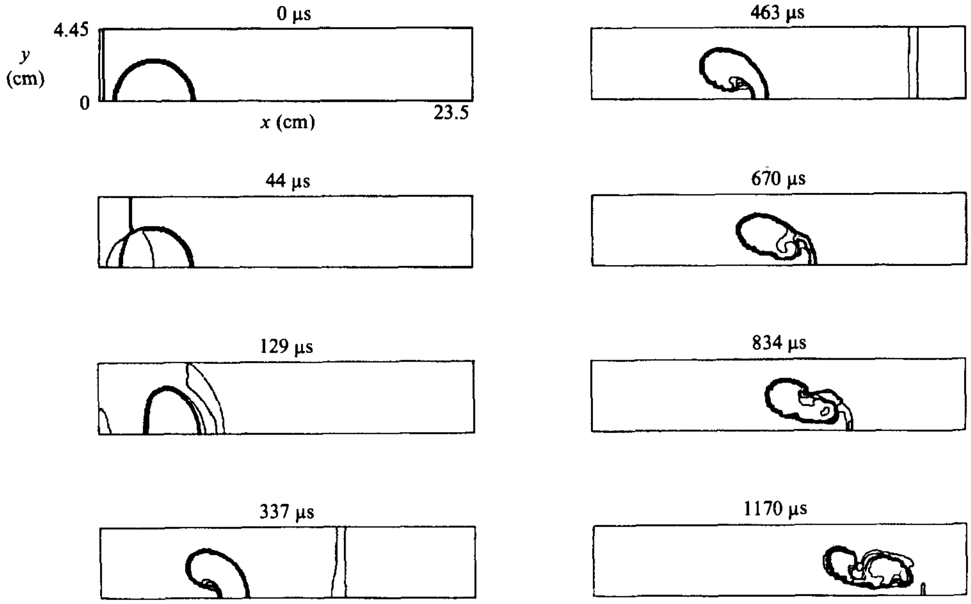

FIGURE 2. Density contours for a planar shock interacting with a 'light' cylindrical bubble. The six contours are evenly spaced over the range from 2.2×10^{-4} to 1.62×10^{-3} g/cm^3. $M = 1.23$.

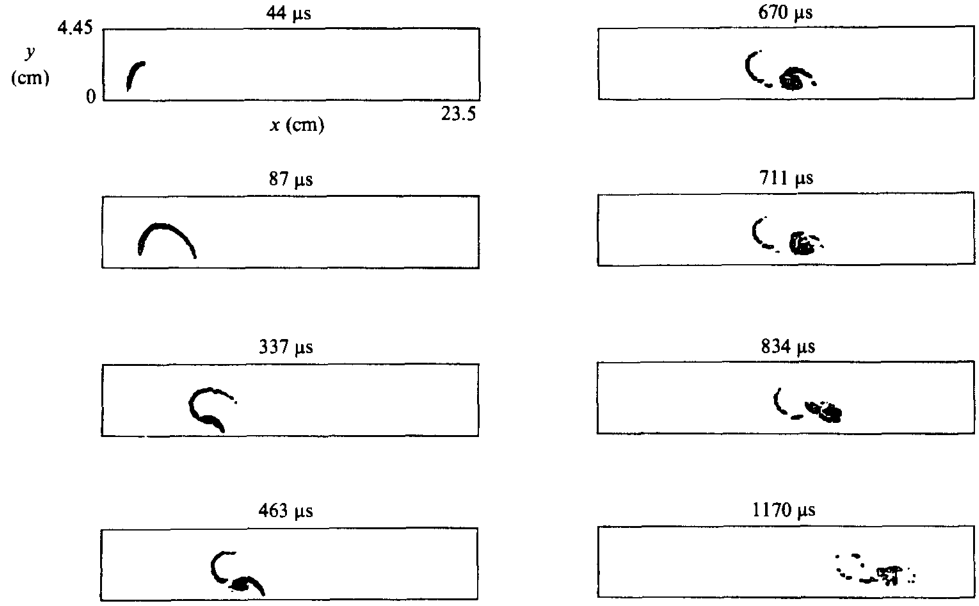

FIGURE 3. Vorticity contours for the cylindrical-bubble case of figure 2. Range: six contours from 2.0×10^4 to 8.0×10^4 s^{-1}.

nonlinear self-interaction of the vorticity field thus causes the emergence of recognizable vortex structures in the fluid after the shock interacts with a local non-uniformity (e.g. a bubble). Notice that the presence of the vortex filament is readily discernible from the vorticity contour plots while the density contours do not clearly indicate the presence of the filament. Figure 3 also shows that the direction of the

Geometry	Structure	Experiment† (m/s)	Simulation (m/s)
Cylinder	Upstream edge	170	198 ± 15
	Downstream edge	145	143
	Jet	230	214
	Vortex filaments	128	135
Sphere	Upstream edge	190	213 ± 30
	Downstream edge	145	154
	Jet	335	331
	Vortex ring	165	175

† Haas & Sturtevant (1987).

TABLE 1. Characteristic velocities for light-bubble cases

vortex roll-up relative to the flow behind the incident shock produces a strong shear which separates some of the vorticity from the filaments. This appears as a 'c'-shaped tail in the vorticity diagrams. Thus the filaments do not contain all of the vorticity that is generated. At later times, weakening and partial breakup of the vorticity field occur.

The density contour diagrams show the features visible in experimental shadowgraphs (Haas, 1984; Haas & Sturtevant 1987). (Our figure represents a slice through the experimental device while experimental photos would show a two-dimensional projection of the three-dimensional density distribution.) The rarefaction wave produced by the acceleration of the shock through the bubble was observed, and the evolving shape of the front of the jet is the same as in the laboratory experiments (figure 2, $t = 463$ μs). The curvature of the shock during passage through the bubble is expected. The times that the phenomena appeared were in good agreement with the data of Haas & Sturtevant. A cascade to significantly smaller-scale structure does not occur in our computer simulations.

A comparison of some of the velocities indicates the quantitative relationship of the calculations to the experimental results. As shown in table 1, the velocities of the jet, the upstream edge of the bubble, and the vortex filaments are consistent with experimental values. The computation of these velocities involves measuring changes in location of the appropriate features over 400 time steps and dividing over the elapsed time (≈ 160 μs). The tables give values derived by averaging over several such intervals. Section 4.6 discusses the uncertainties shown in tables 1 and 2. The version of the paper by Haas & Sturtevant (1987) to which we have referred did not provide estimates of the experimental uncertainties, although §4.6 touches upon that aspect as well.

4.2. *Light spherical bubble*

Figures 4 and 5 show density and vorticity contour diagrams for the case of a planar shock ($M = 1.25$) passing through the upper half of a spherical bubble ($D = 45$ mm) filled with a gas that is less dense than the ambient gas. The initial conditions behind the planar incident shock were $\rho_2 = 1.84 \times 10^{-3}$ g/cm^3, $P_2 = 1.68 \times 10^6$ dyne/cm^2 and $V_2 = 1.24 \times 10^4$ cm/s. As predicted by (1), the shock again produces vorticity at the interface of the bubble with the ambient gas. The associated rotational fluid motion causes a fluid jet through the bubble and rolls the vorticity into a vortex ring.

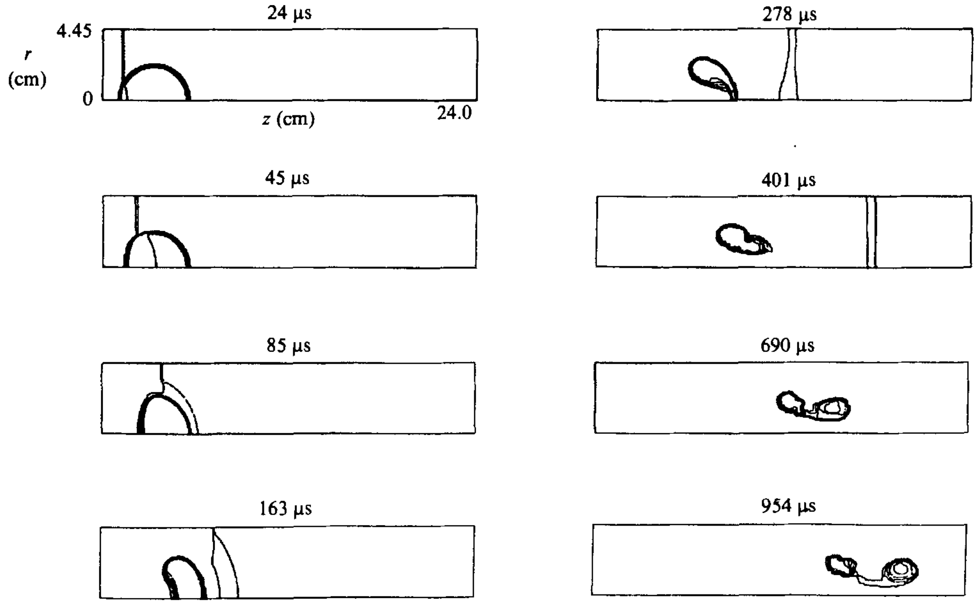

FIGURE 4. Density contours for a planar shock interacting with a light spherical bubble. Range: same as in figure 2. $M = 1.25$.

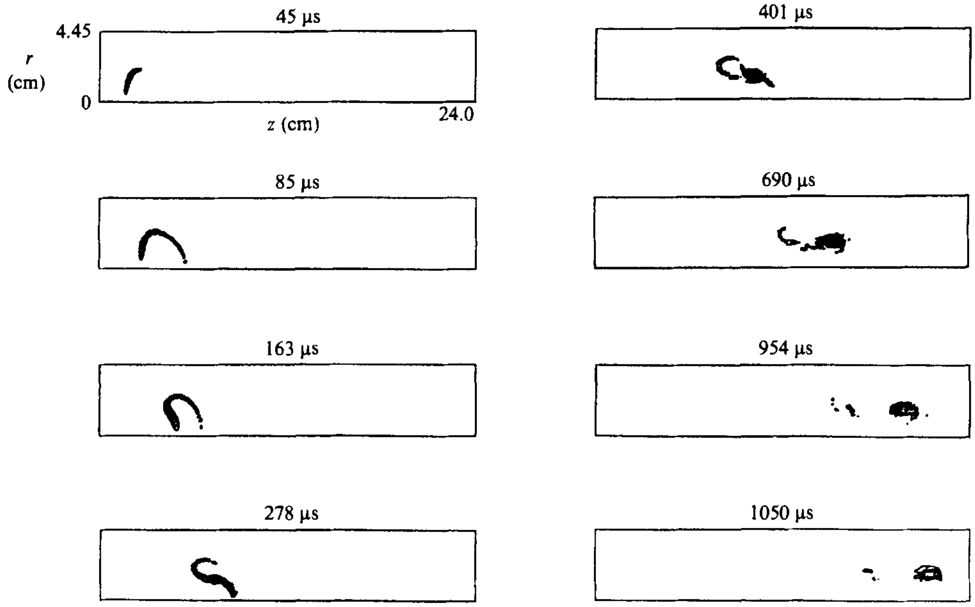

FIGURE 5. Vorticity contours for the spherical-bubble case of figure 4. Range: same as in figure 3.

This represents a nonlinear interaction of the vorticity with itself as mediated by the fluid. In contrast to the cylindrical-bubble case, the roll-up is faster and tighter, producing higher velocities. Consequently, the vortex ring propagates more quickly away from the remainder of the bubble and appears prominently in the density contour diagrams. The vorticity dynamics that lead to the vortex-ring formation and

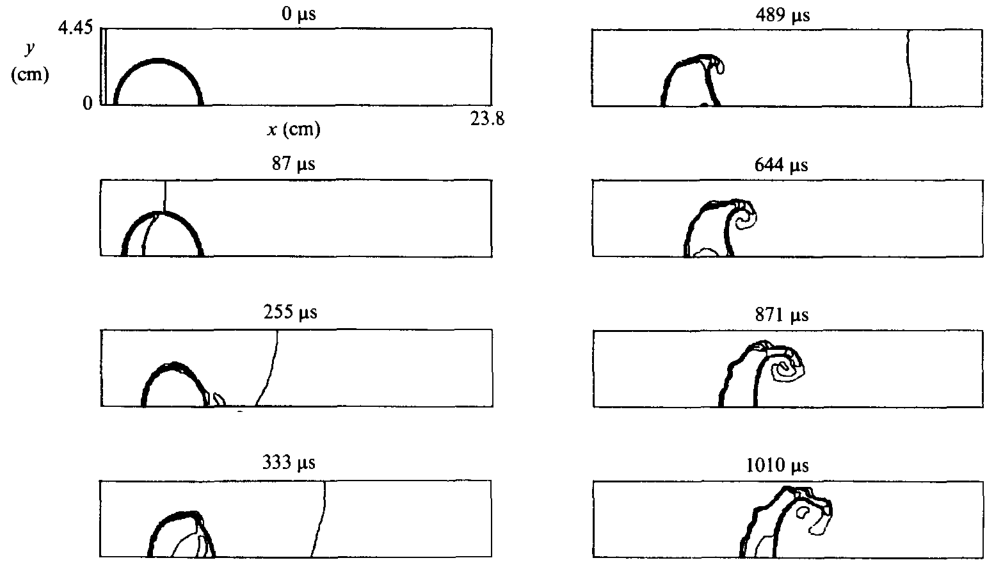

FIGURE 6. Density contours for a planar shock interacting with a 'heavy' cylindrical bubble. Range: six contours from 1.35×10^{-3} to 6.00×10^{-3} g/cm^3. $M = 1.23$.

separation from the bubble are, however, difficult to ascertain from the density contours alone. Table 1 again shows good agreement between velocities observed in the experiments of Haas & Sturtevant and our numerical simulations.

Regarding the vortex strength produced by the shock, note again that the rapid passage of the refracted shock through the bubble ($t = 85$ μs) produces primary and secondary transmitted shocks which intersect the (diffracted) incident shock well before the latter traverses the downstream half of the bubble. As in the cylindrical case, the alignment of the refracted shock and the downstream portion of the bubble is considerably greater than in the case of a perfectly planar shock. These factors once again reduce the generation of vorticity over the downstream half of the bubbles as compared to the upstream half. Section 4.5 discusses this further.

4.3. '*Heavy*' *cylindrical bubble*

Figures 6 and 7 show density and vorticity contour diagrams, respectively, for a planar shock interacting with a cylindrical bubble containing a gas mixture which is more dense than the ambient gas ('heavy' cylindrical bubble). The initial conditions are the same as for the light-cylindrical-bubble case, except that the density of the gas inside the bubble is 4.64×10^{-3} g/cm^3 (Haas 1984). This is the value for the mixture of Freon-22 and air reported to us by Haas at the time our calculations were performed (see Haas 1984). Later the value was corrected to 3.69×10^{-3} g/cm^3 (Haas & Sturtevant 1987). This difference does not materially affect our comparisons with the experimental observations. Section 4.6 addresses the difference further.

The vorticity contour diagrams show that negative vorticity is produced along the upper edge of the bubble, excluding the portions near the axis of the shock tube. Along the axis, the pressure gradient of the shock and the density gradient at the edge of the bubble are aligned, so our theory predicts that little vorticity will be produced there. The vorticity is opposite in sign from the light-bubble case because the density gradient is radially inward for the heavy bubble, making the source term

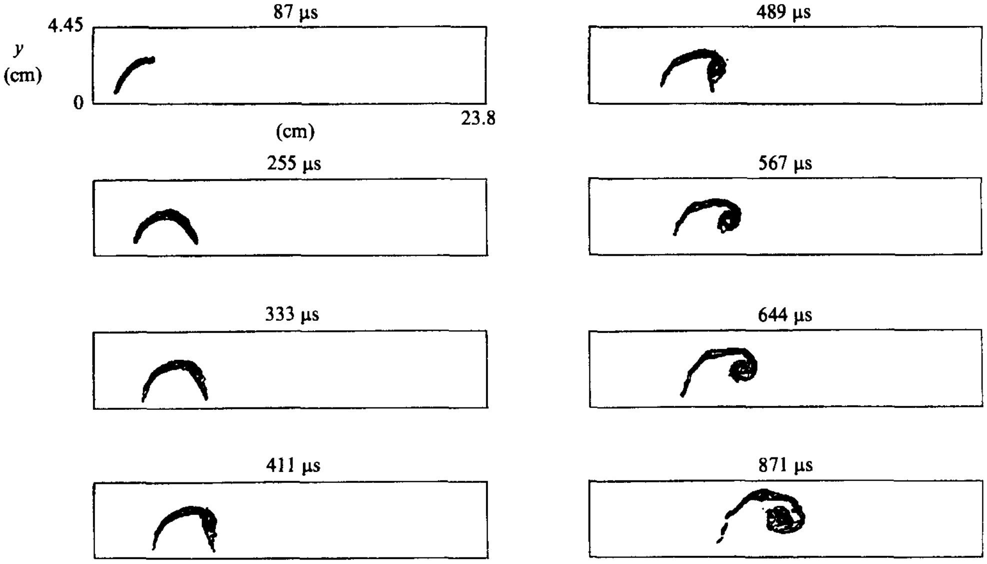

FIGURE 7. Vorticity contours for the cylindrical-bubble case of figure 6. Range: six contours from -5.0×10^4 to -1.0×10^4 s^{-1}.

in (2) negative along the upper edge. By symmetry, positive vorticity resides along the lower bubble surface. As in the case of the light bubble, the vorticity generation appears to track the fastest shock, in this case the diffracted incident shock outside the bubble. Because the refracted wave is curved in the same manner as the upstream edge of the bubble, we expect less vorticity generation relative to a planar shock, according to (2). In addition, diffraction of the incident shock and the complicated interaction of interior waves with the downstream edge of the bubble will cause deviations from a simplified model with planar shocks traversing the interior and exterior of the bubble. The values of the vortex strength computed from the simulations are smaller owing to these factors (§4.5).

For bubbles that are more dense than ambient, the associated rotational motion opposes the flow behind the incident shock, causing significant differences relative to the light-bubble case. As is evident from figures 6 and 7, no large jet is induced by the rotational flow. However, the vorticity, through the medium of the fluid, does spiral into a filament pair at the outer downstream edges of the bubble. The filaments are more easily seen in the density contour diagrams than for the case of light bubbles. Here, as opposed to the light-bubble case, the flows behind the incident shock do not set up a shear which could cause the tail of the spiral to separate from the filament. Thus the spiral remains intact. Notice that the tail of the spiral retains its initial length even though the vortex filament appears to be rolling up throughout the simulation. This most likely indicates straining of the fluid by rotational motions embedded in the flow associated with the incident shock. Another possibility is that more vorticity is being generated, perhaps initially by rarefaction waves propagating backward from the downstream edge of the continually deforming bubble. A slowly growing impulsive Rayleigh–Taylor (Richtmyer–Meshkov) instability at the upstream interface of the bubble also contributes vorticity there (last paragraph of this section).

The density contour diagrams track the experimental photographs closely. Although our interest is primarily in the development and effects of the large-scale

Geometry	Structure		Experiment† (m/s)	Simulation (m/s)
Cylinder	Upstream edge	(early)	73	68 ± 22
		(late)	90	91
	Downstream edge	(on axis)	78	65
		(off axis)	130‡	130
	Vortex filaments		130‡	98
Sphere	Upstream edge	(early)	60	67 ± 22
		(late)	99	86
	Downstream edge	(early)	83	91
		(late)	100	110
	Jet	(early)	165	91
		(late)	123	—
	Vortex ring		—	79

† Haas and Sturtevant (1987). ‡ See text.

TABLE 2. Characteristic velocities for heavy-bubble cases

vorticity field, note that a different sort of 'jet' does occur in the heavy-bubble case. This jet results from the convergence of the refracted shock inside the bubble on the downstream edge at the axis (Haas & Sturtevant 1987), causing a pressure peak which pushes the bubble gas quickly downstream for a short time. The solution following convergence of the refracted wave, in fact, resembles a shock wave emanating from a point source, producing curved pressure waves interior and exterior to the bubble (Löhner *et al.* 1988). Evidence of the exterior wave is visible in figure 6 as a small density peak on axis behind the shock at $t = 225$ μs. In subsequent snapshots, a 'back-reflected' wave appears in the interior (Haas & Sturtevant 1987). This structure follows the expanding interior pressure wave that was present at $t = 255$ μs. The interior pressure wave itself does not appear in our density contour plot at 255 μs because the (shocked) interior of the bubble at that time is higher in density than our maximum contour level. A weak rarefaction appears in the interior on the axis at time $t = 489$ μs; the wave spreads by $t = 644$ μs. This rarefaction wave is apparently a remnant of the radial expansion described above. Eventually the bubble strikes the edge of the shock tube some time after 1 ms. To study quantitatively the jet and related wave phenomena inside the bubble requires better resolution. Such calculations are the subject of a subsequent paper (Löhner *et al.* 1988).

Table 2 shows a comparison of our numerical determination of various velocities with the experimental values of Haas & Sturtevant. This table goes beyond our main purpose of describing the physics of vorticity generation by the shock–bubble interaction. The inclusion of these numbers, however, can help us to detect significant differences between the laboratory experiments and our numerical simulations. Section 4.6 discusses the uncertainties shown in table 2.

This subsection focuses on the upper half of the table (heavy cylindrical bubble). The agreement between the experiments and the simulations is good in nearly all cases. Of interest is the velocity of the vortex filaments. If one uses the downstream edge of the apparent vortex filament in the density contour plots, one arrives at a value of approximately 130 m/s. This is somewhat greater than the flow velocity just upstream of the shock (114 m/s), indicating that the interaction with the shock-tube wall was perhaps more important than the counterflow due to the vortex in the lower half of the system. However, using the vorticity contour plots, one obtains 98 m/s, which is more in line with the expectation that the counterflow of the other real vortex is more significant. The value given by Haas & Sturtevant seems to signify the velocity of the apparent downstream edge of the vortex filament (i.e. the 'off-axis' portion of the bubble). Our calculations show that the motion of the vortex filaments is not precisely discernible from the motion of the downstream 'off-axis' portion of the deforming bubble.

Ripples occur on the upstream edge of the heavy bubble. This is apparently the linear Richtmyer–Meshkov or impulsive Rayleigh–Taylor instability. Such distortions were also present in the experiments of Haas & Sturtevant and have been confirmed in recent highly resolved calculations with a new compressible finite-element code (Löhner *et al.* 1988). The finite surface tension in the experimental bubble should suppress the growth of the instability to some extent. In the case of the light bubble, the vorticity-induced jet destroyed the upstream surface and thus no similar ripples occurred. The presence of rarefaction waves propagating backward, the stretching and distortion of the bubble by the vortex motion, and the forward flow associated with the incident shock most likely render the upstream edge more susceptible to linear instability. According to (2), the rippling of the upstream surface could permit the generation of vorticity by the rearward-propagating rarefaction waves observed in the simulation. The vortex strength in the upper half-plane did increase slowly and steadily with the passage of time. The final frames of figure 6 show evidence of smaller-scale structure in the density field.

4.4. *Heavy spherical bubble*

Figures 8 and 9 show density and vorticity contour plots for the case of a planar shock ($M = 1.25$) passing through the upper half of a spherical bubble ($D = 45$ mm) filled with a gas that is more dense than the ambient gas. The gas mixture has the same properties as in the cylindrical case. The shock–bubble interaction again produces vorticity at the edge of the bubble except near the axis. The rotation associated with the vorticity causes a portion of the bubble and the local ambient gas to roll into a ring with a spiral cross-section. The vorticity follows the fluid to form a vortex ring. The phenomenological effects of shock curvature and diffraction on the generation of vorticity are the same as for the heavy cylindrical bubble discussed in §4.3, as are the vortex roll-up and evolution.

Again the density diagrams in figure 8 track the experimental features closely. The refracted shock focuses at a point just inside the downstream edge of the bubble ($t = 171$ μs). The external diffracted shock reaches the shock-tube axis just before the focusing is complete. The focusing produces a pressure peak which results in a radial expansion similar to a shock wave emanating from a point source. This initiates an outward jet at the edge of the bubble and also causes a rearward-propagating pressure wave (not shown) and a subsequent rarefaction ($t = 246$ μs, 327 μs), as discussed in a previous section. The jet in the spherical case appears later as a well-defined spike, as opposed to the cylindrical case, in which the jet was much less apparent. Also worth noting is the weak density peak that appears on axis inside the downstream edge at $t = 490$ μs. This appears to be forward-moving shock produced by the interaction of the rearward-propagating rarefaction wave with the upstream edge of the bubble (Landau & Lifshitz 1959). Note that the vortex structure does not stretch toward the shock-tube walls and instead remains compact, in constrast to the cylindrical case.

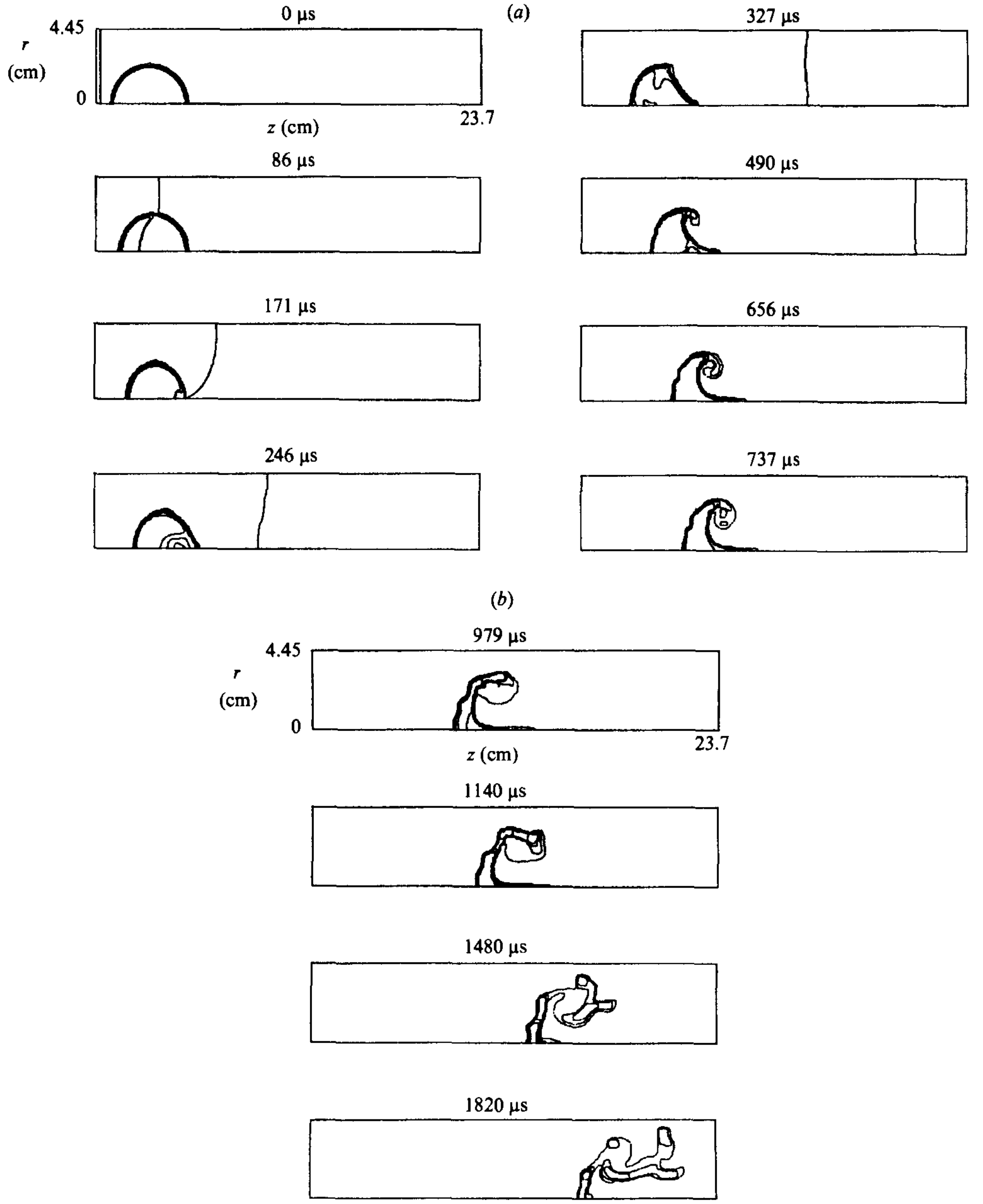

FIGURE 8. Density contours for a planar shock interacting with a heavy spherical bubble. Range: same as in figure 6. Part (*b*) applies to later times. $M = 1.25$.

Table 2 shows good agreement of the velocities of various features, as derived from experiment (Haas & Sturtevant 1987) and from our simulations. The only major discrepancies are the velocity of the vortex ring, which could not be determined experimentally, and the velocity of the jet, which is again caused by focusing of the refracted shock at the downstream edge. As the density contour diagrams in figures 6 and 8 show, the jet is more pronounced for the spherical bubble and appears as a spike along the axis at the downstream edge. Eventually the rotational motion of the vortex ring pulls fluid away from the axis and the spike along the axis recedes. The

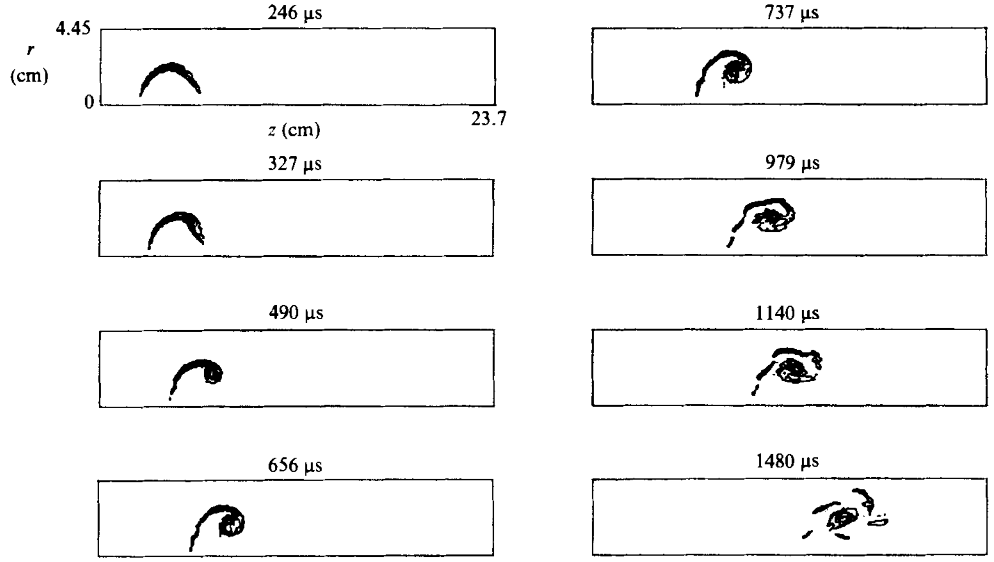

FIGURE 9. Vorticity contours for the spherical-bubble case of Fig 8. Range: same as in figure 7.

experiment showed a far more pronounced spike, and the velocity was initially quite large (165 m/s), finally relaxing to the flow velocity behind the incident shock. This difference between the numerical simulation and the laboratory experiment may be due to insufficient resolution in the computer calculation of the refracted and internal diffracted waves. Section 4.6 covers other possible causes.

At late times, as shown by the density contours in figure 8(*b*), the region near the vortex ring breaks up into smaller-scale features that are eventually stretched horizontally into finger-like shapes by the flows associated with the incident shock. This fingering is also prominent at late times in the experimental photos of Haas & Sturtevant. Apparently the transition to smaller scales (figure 8*b*) decreases the coherence of the rotational flows, permitting the flows associated with the planar shock to stretch the bubble locally. The late-time diagrams also show evidence of Richtmyer–Meshkov instability on the upstream surface of the spherical bubble. This might contribute somewhat to the creation of the finger-like structures by introducing local alterations in the density and vorticity fields at later times.

4.5. *Vortex strength*

Equation (4) gives the vortex strength generated by the interaction of a shock with a light or heavy bubble, assuming that the shock remains planar throughout the interaction. The numerical simulations and laboratory experiments have shown that the incident shock is diffracted by the bubble and that a curved refracted shock traverses the interior of the bubble at a different speed than the diffracted incident shock. The preceding sections have presented arguments, based on our theory as embodied in (1) and (2), stating that the distortion and interaction of the various shocks will reduce the vortex strength relative to (4). Equation (4), however, still provides a useful means of predicting the vortex strength corresponding to a given set of shock and bubble parameters. Table 3 shows the values of vortex strength resulting from our theory, embodied in (4), and from the numerical simulations. The numbers verify the above ideas.

The table presents two methods of computing the vortex strength from the

			Simulation	
Bubble type	Geometry	Theory [equation (4)]	A†	B‡
Light bubble	Cylinder	9.1	4.8	3.2
	Sphere	8.5	6.5	4.3
Heavy bubble	Cylinder	−6.5	−5.5	−4.0
	Sphere	−6.1	−3.5	−3.5

† Direct determination of circulation in the upper half-plane just after shock has passed through bubble.

‡ From axial velocity at location of vortex filament or ring.

TABLE 3. Vortex-strength calculations m^2/s for upper half-plane

numerical simulations. The first, A, is an integration of the vorticity over the upper half-plane, which contains one vortex filament or one cross-section of a vortex ring. The other indicator of the amount of vorticity present is the flow velocity induced by the vortex structures after the roll-up phase. For the cylindrical case, the vortex filaments will induce a velocity along the axis of the shock tube given by

$$v_z(z) = \frac{\kappa d}{\pi(z^2+d^2)}, \tag{6}$$

where d is the perpendicular distance of the centroid of each filament to the shock-tube axis (axis of symmetry) and z represents position along the axis relative to the line joining the filament pair. The expression in (6) comes from differentiating the stream function for a set of discrete vorticites (Batchelor 1967, p. 530). In the case of a vortex ring, the velocity induced along the axis is

$$v_z(z) = \frac{\kappa d^2}{2(z^2+d^2)^{\frac{3}{2}}}, \tag{7}$$

where d and z are the same quantities as in (6). The expression in (7) comes from differentiating the stream function for a vortex ring (Batchelor 1967, pp. 78, 521). Equations (6) and (7) show that, for the same strength κ, the local velocity field of a vortex ring is roughly 50% faster than that of a filament pair. The velocities induced on the shock-tube axis will provide values of the vortex strengths through the use of (6) and (7) for $z = 0$. Subtracting the flow velocity behind the incident shock from the axial velocity measured at the centre of the vortex-filament pair or vortex ring gives an approximate velocity induced on axis by the vortices. Table 3 (column B) shows the vortex strengths inferred in this manner from the numerical simulations. In the light-bubble cases, the vortex filaments contained approximately 66% of the total circulation produced. This is consistent with figures 3 and 5, which show that shear forces broke the distribution of vorticity into two parts in the upper half-plane. For the heavy cylindrical bubble, the filaments contained approximately 73% of the initial circulation. For the heavy spherical bubble, the vortex-ring circulation was approximately equal to the initial circulation produced by the shock–bubble interaction. These higher figures are consistent with the observation that shear forces did not break the early-time vorticity distribution into pieces. Thus the roll-up of vorticity continued throughout the calculation. In addition, the circulation was increasing slowly with time during the calculation, permitting a further increase in strengths of the vortex structures. Apparently because the vortex ring did not stretch toward the wall, instead remaining compact, the intake of vorticity was more efficient than in the cylindrical case.

4.6. *Uncertainty in results of laboratory and numerical experiments*

In analysing the results of numerical simulations, one must be careful to differentiate between sources of error in the numerical algorithm and uncertainties in the values of physical quantities derived from the numerical-simulation data. A final category of analysis deals with the degree of similarity between the situation modelled in a numerical experiment and the actual conditions in the laboratory. The paragraphs below discuss each factor in the context of the present problem.

Errors in the numerical algorithm derive from mathematical considerations. The key issue for algorithms in computational fluid dynamics is how well the numerical solution, based on finite information (e.g. values at a finite number of spatial and temporal points) approximates the solution of the governing differential equations in a continuous spatial and temporal domain. To characterize an algorithm, one describes the order of the truncation error, the phase accuracy, and other properties, such as the order of dissipation, as we have done in § 3.1 for FCT. Tests for stability and resolution requirements are also essential and have been performed extensively for FCT. The Appendix reviews the types of algorithms that might be appropriate for studying vortex generation by shock–bubble interaction and shows that FCT is representative of the most cost-effective class of algorithms at this time.

The second source of uncertainty in numerical simulations comes from treating the resulting numbers as data coming from a numerical *experiment*. To obtain the velocity of a particular feature in the flow, for example, one must locate that feature in each 'snaphsot'. This is true whether the data are in the form of shadowgraphs from a laboratory experiment or density contour diagrams from a numerical simulation. The second type of uncertainty is therefore common to both laboratory experiments and numerical simulations. Neither measurement is exact, and for reasons given below, the present authors have attributed the particular uncertainties to the simulation velocities shown in tables 1 and 2 and expect similar magnitudes for uncertainties in the laboratory experiments.

Each of the velocities in tables 1 and 2 relates to the speed of an interface or a structure (vortex or jet). As explained in §3.1 and the Appendix, the FCT algorithm smears discontinuities over approximately three grid cells. Thus the uncertainty in the speed of a given interface is the uncertainty (approximately ±3 cells) in the distance that the interface travels between two snapshots divided by the time interval between snapshots. In the laboratory experiments, shadowgraph photos corresponding to different times were obtained by running separate experiments that were as nearly identical as possible (J.-F. L. Haas 1983, private communication). Thus the speed of a given feature was uncertain because different shocks and bubbles were used to show the conditions at different times, leading to both spatial and temporal inaccuracies. Another factor also contributed to uncertainties in both the numerical simulations and the laboratory experiments. Because the boundaries of the shock tube were close to the bubble and because the vorticity distribution and the fluid were continually evolving, the flow was unsteady at all times. Attributing one velocity to an evolving interface or structure can only have significance as a *characteristic* velocity scale and should not apply to the speed over a long time interval. To account for all of these sources of uncertainty, we averaged the values derived from several time intervals and then computed the standard deviation. This standard deviation was close to the number computed from the ± 3-cell-location uncertainty described above. The larger of the two appears in tables 1 and 2 for each type of bubble.

A final topic to be covered in this subsection is the set of differences between the numerical model (§ 3.2) and the laboratory experiments. In all cases, the effects on the phenomenological observations were minimal, as the good agreement in tables 1 and 2 shows. The differences and their consequences are as follows:

(i) The ideal-gas equation of state with $\gamma = 1.4$ did not account for the different value of γ in the bubble gas. Our experience has shown that more realistic equations of state have only small effects on the phenomenology of shock physics (e.g. Book *et al.* 1981). Since weak shocks are involved here ($M \approx 1$), the error in the fluid velocity when $\gamma \neq 1.4$ should vary roughly as $(\gamma/1.4)^{\frac{1}{2}}$. In fact, Landau & Lifshitz (1969) provide a more detailed analysis which gives somewhat smaller error estimates: approximately 8% for the light bubble ($\gamma = 1.67$) and 3% for the heavy bubble ($\gamma = 1.31$).

(ii) The model does not include the effects of surface tension. This should render the bubble surface somewhat less stable, as comparisons with experiment have shown. Again, however, these effects are small.

(iii) The model is two-dimensional and cannot faithfully represent the experimental apparatus or three-dimensional instabilities and small-scale processes. For example, the test section of Haas & Sturtevant had a square cross-section which could not be represented in our model. This would affect waves that reflect from the test-section walls, producing secondary interactions with the bubble. The inability to represent three-dimensional instabilities and small-scale processes can also have effects on the large-scale dynamics of the vortex structures and the structuring of vortex cores (V. A. Kulkarny, private communication, 1987).

(iv) The numerical simulations permit more extensive diagnostics. Especially important is the ability to determine the vorticity distribution directly, so that vortex structures and their characteristic velocites could be obtained. The characteristics of the vorticity were not as obvious in the experimental shadowgraphs nor were the velocities of the vortex structures as easily determined from the experiments (see table 2).

(v) In cases for which the bubble gas was heavier than the ambient air, the experimental bubble was more like a teardrop than a sphere in shape (Haas 1983, 1984 ; Haas & Sturtevant 1987). This could lead to stronger focusing of the refracted shock and a stronger initial impulse to the jet in the heavy-spherical-bubble case.

(vi) The teardrop shape of the laboratory bubble contributes in another way to the observation of a more exaggerated jet in the laboratory experiments than in the simulations. Over a significant portion of the laboratory bubble, the misalignment between the density gradient of the bubble and the pressure gradient of the incident shock was less than for the perfect sphere that was present in the numerical simulations. Equation (2) shows that the resulting vortex strength is lower when the misalignment is less. The vortex motion opposing the jet is thus less effective in reducing the speed of the jet in the laboratory experiments than in our simulations (§ 4.4). The experimental photos of Haas & Sturtevant give some indication that this is so.

(vii) The simulations of the heavy-bubble cases used a bubble density of 4.64×10^{-3} g/cm^3 rather than the last reported experimental value of 3.69×10^{-3} g/cm^3. Equation (4) of our theory permits the assessment of the differences between the simulations and experiments due to this discrepancy. The other variables being approximately the same, the ratio of vortex strengths for bubble densities ρ_{01} and ρ_{02} is then

$$\frac{\kappa_1}{\kappa_2} \approx \frac{\ln(\rho_\infty/\rho_{01})}{\ln(\rho_\infty/\rho_{02})}. \tag{8}$$

Since the induced velocities are proportional to κ, the vortex contributions to the velocity field should be 20% lower in the experiment in comparison to our simulations. From (6) and (7) and the values of the vortex strength inferred from the velocity field of the simulations (table 3, column B), this should amount to $\approx$ 10 m/s at the axis of the shock tube and less elsewhere. Given the value of $\approx$ 120 m/s for the flow behind the incident shock, differences of less than $\approx$ 10% could appear in the characteristic velocities of table 3. Very near the vortex structures, the differences should be even smaller because of boundary effects. In the cylindrical-bubble case, for example, the real vortex filament in the upper half-plane experiences the flow field of the vortex filament in the lower half-plane and the flow induced by the image vortex corresponding to the upper boundary. The latter two fields are oppositely directed, so that the effect on the velocity of the vortices is reduced.

5. Summary

The primary goal of this work has been to explore theoretically and numerically the simplest case of a shock interacting with a fluid containing discrete inhomogeneities: the case of a single isolated inhomogeneity. The emphasis has been on the generation and dynamics of long-lived vorticity by such processes. The experiments of Markstein (1957*a*,*b*) and, in particular, Haas (1983, 1984) and Haas & Sturtevant (1987) have provided excellent points of reference for an investigation of the effects of geometry and density of the inhomogeneity relative to the ambient medium. This paper has shown that residual vorticity is generated at the edge of the inhomogeneity except near the axis, in accordance with our nonlinear theory, based on (1), (2) and (4). The vorticity dominates much of the late-time dynamics of the entire system. Further, the vorticity interacts nonlinearly with itself through the medium of the surrounding fluid, producing distinct vortex structures, depending on the geometry of the inhomogeneity. These structures were difficult to ascertain from the density diagrams and experimental shadowgraphs in most cases, but were readily determined in the vorticity diagrams. The nonlinear self-interaction picture provides an alternative and a more attractive theoretical point of view than linear impulsive Rayleigh–Taylor theory. The nonlinear analytic model gives a value for the vortex strength that explains a decrease in the normalized vortex-structure propagation velocities with increasing Mach number of the incident shock, unlike other theories.

Equally as interesting, but not examined as closely in this paper, were the refraction, reflection, and diffraction of the shock by the inhomogeneity at early times in the experiments and simulations. The simulations have demonstrated the effects associated with the divergence of the shock within the lighter bubble and the focusing by the heavier bubble. We are now performing calculations with optimum resolution of the various wave structures associated with the early-time phenomena (Löhner *et al.* 1988). Haas & Sturtevant (1987) have thoroughly discussed the qualitative features and experimental wave parameters for the behaviour at early times.

The authors gratefully acknowledge support from the Office of Naval Research and helpful discussions with David Bacon, Brad Sturtevant, Jean-Francois Haas, George Markstein, Raafat Guirguis, Rainald Löhner, and Russell Dahlburg. We particularly appreciate the effort of Steve Zalesak in reviewing the Appendix on numerical methods and in making suggestions for improvement. Dr Haas and Professor Sturtevant also deserve special mention for providing copies of experimental photographs, Dr Haas's Ph.D. thesis, and a preprint of their paper (Haas & Sturtevant 1987). We thank Dr V. A. Kulkarny for helpful remarks regarding approaches to the general problem and the effects of local and three-dimensional instabilities and small-scale processes on structuring of vortex cores. Fred Rettenmaier of the NRL Library has also provided invaluable assistance in obtaining vital publications. We thank Robert Ahearne for his assistance in analysing the simulation data and Michele A. Guarneiri and Nancy Ciatti for a superb typing and editorial job on the initial versions of this paper.

Appendix : Survey of numerical algorithms

The present problem is a very difficult one from a numerical point of view, involving non-steady compressible flows (shocks) which generate non-steady, complex rotational flows embedded in a compressible medium. In addition, the system boundaries are nearby. The presence of two fluids of different density separated by sharp interface (bubble boundary) is a further complication. Most numerical treatments of evolving rotational flows have treated the flows in isolation, assuming incompressibility, and are totally inappropriate in the present context. Our discussion must, therefore, begin with algorithms that treat shocks adequately. One cannot, of course, expect the algorithms used most often for problems containing shocks (i.e. those algorithms that have been thoroughly explored and optimized) to be the best for rotational flows as well. Thus the discussion will cover algorithms that are presently under development and that offer some hope of optimum treatment of both shocks and the complex rotational flows generated by them.

Algorithms for treating shocks are of two general types: 'shock-fitting' schemes and 'shock-capturing' schemes. For two-dimensional flows, shock-fitting or 'front-tracking' methods (Richtmyer & Morton 1967; Chern *et al.* 1986) compute the locations of physical waves in the fluid through the use of a system of curves associated with the waves. Front-tracking codes also use a two-dimensional finite-difference grid along with conditions at the bounding surfaces and waves to determine properties at other points in the flow. Recent results for simple supersonic flows (e.g. regular reflection of an oblique planar shock) and Kelvin–Helmhoz instability problems with velocity jumps of Mach number 0.1 to 1.0 have been excellent (Chern *et al.* 1986). In addition to the need to maintain extensive data structures, the main problem with this method appears to be the need for a general solution to the two-dimensional Riemann problem. The latter involves the development of a complete list of elementary wave interactions for the problem being simulated. Apparently the prospects for this approch to multidimensional flow have become much better due to the progress shown by Chern *et al.* However, we must presently classify front-tracking methods as still under development relative to the shock-bubble interaction problem. Because our problem involves a sharp interface between the bubble and the ambient gas, the front-tracking methods should be of great interest once the algorithms have been fully developed and optimized.

The other type of algorithm for handling shocks is called 'shock capturing' and again uses a finite-difference grid. In these calculations, shocks are smeared out on the grid to prevent non-physical numerical oscillations (Richtmyer & Morton 1967). Usually other discontinuities (e.g. interfaces between different materials) will be smeared out over a small number of grid cells as well, so that the locations of intefaces will be uncertain to that extent. Woodward & Colella (1984) have given an excellent review of the most well-known classes of shock-capturing algorithms, including descriptions, tests, and comparsions of representatives of each class. The classes are as follows: artificial-viscosity methods, linear hybridization, and Godunov's approach.

The first category is also the oldest and involves adding enough artificial viscosity to the hydrodynamic equations to ensure smoothness of the solution at discontinuities. This is also the most expensive technique because very fine grids (large numbers of grid points in the physical domain) are required to ensure convergence of the solution. On coarse grids, the non-physical viscosity degrades the solution prematurely. Continuously adaptive meshes have been used to place the finest grid cells near the thinnest features in the flow to minimize the expense of an accurate calculation. Unfortunately such schemes require an implicit treatment of the flow and thus are quite slow. In addition, the schemes are quite complex in two or more dimensions (Woodward & Colella 1984).

Linear hybridization blends a high-order finite-difference scheme with a low-order scheme, as described in an earlier section (3.1) on flux-corrected transport. Taken separately, a high-order (second-order or greater) scheme gives high accuracy in smooth flow but produces numerical oscillations or instability at discontinuities. A low-order algorithm with sufficiently large dissipative truncation errors will produce smooth (monotonic) profiles at discontinuities but will suffer from the same limitations as the artificial viscosity algorithms described above. Properly mixed, the high- and low-order portions of the hybrid scheme place the largest dissipation in the vicinity of discontinuities to maintain smoothness while giving high accuracy everywhere else. Usually discontinuities are smeared over 2–3 cells by this procedure. The use of the high-order scheme elsewhere prevents discontinuities from spreading over more than 2–3 cells throughout the calculation. Flux-corrected transport was the first of these algorithms that worked really well and has been successfully (and easily) applied to the largest range of problems, including those with strong shocks (Book *et al.* 1981) and others with nonlinear instability in subsonic shear flows (Grinstein *et al.* 1986). Thus the FAST2D code has previously provided excellent results on both types of phenomena involved in shock-bubble interactions. The most recent hybrid finite-difference algorithm under development is the 'total-variation-diminishing' scheme of Harten (1983) and Yee (1987). For the same computational price on the same problem, these schemes should not give large improvements over the second-order FCT algorithm in FAST2D, although they are in principle more general and flexible. Another subcategory worthy of mention is the two-dimensional, fully compressible, finite-element code being developed by Löhner (1987) and Löhner *et al.* (1987), which uses an unstructured, adaptive, triangular grid to produce optimum resolution of all waves and interfaces.

The last category of successful two-dimensional algorithms have built on Godunov's approach, piecing together discontinuous solutions based on Riemann's shock-tube problem. The latest and most successful of these is the piecewise parabolic method (PPM) of Colella & Woodward (1984). The PPM algorithm is particularly good for very strong shocks. The drawback of the method is the much greater complexity of the code. For studying the phenomenology of the interaction between a weak shock and a bubble, the increased complexity of the code may not be cost-effective. The Riemann solver, which improves the treatment of wave interactions will be of little advantage for studying the rotational flows present after the shock has left the vicinity of the bubble. At that point wave interactions will be much less important. Also, the complex wave structures present during the interaction might require a much more general multidimensional Riemann solver than is currently included in PPM. As indicated above, shock-fitting algorithms can suffer from this problem as well.

To complete the discussion we should briefly consider algorithms that handle rotational flows well and indicate which approaches might provide an optimum treatment of the problem at hand. Finite-difference algorithms must necessarily be limited to those given above. Worthy of mention, however, is the SPLISH code (Fritts & Boris 1979; Fyfe, Oran & Fritts 1989). SPLISH is Lagrangian, applies to incompressible flows, and features a dynamically restructuring, triangular grid to resolve interfaces exceptionally well. A compressible version of the code might be optimum for this problem. In addition to finite-difference schemes, the two methods most often used have been 'vortex methods' and spectral methods. The vortex methods (Leonard 1980) include the following: point vortices, vortex blobs, contour dynamics, and vortex-in-cell methods (including cloud-in-cell methods). The greatest limitation for our purposes is that these methods have been designed for incompressible fluids only. That any vortex method would alone form the basis for modelling the interaction of a shock with a bubble is presently unthinkable. Proposals have been made for a hybrid code incorporating a shock-capturing algorithm and a vortex method to handle the different components of a complex compressible flow field (R. Guirguis, 1986, private communication). Such a code is years away from practical application. One might also attempt to use a compressible finite-difference code for the time interval over which the shock interacts with the bubble and then switch to a vortex method to compute the evolution of the flow field after the interaction. This would imply that the late-time flow field was incompressible. The applicability and development of such a method would itself form an interesting and challenging field of research.

Spectral algorithms are far more promising than vortex methods at this time (Gottlieb 1985). These techniques involve expansions of the flow variables in terms of appropriate functions and then solving sets of ordinary differential equations for the expansion coefficients. The most successful applications to date have involved incompressible fluids with vortex structures and incompressible turbulent flows. However, both shock-capturing and shock-fitting spectral algorithms have been developed and applied to specific problems. The primary drawback is that shock waves can produce numerical oscillations throughout the grid, and the solution can be quite unstable (Gottlieb, 1985). Approaches to this problem include the addition of artificial viscosity and the use of special filters at regular intervals. Clearly much more work is necessary to develop a practical spectral algorithm with applications to a wide range of compressible flows.

This discussion shows that linear hybrid shock-capturing schemes, such as the FCT algorithm which we use, are presently the most cost-effective and reliable for multidimensional modelling of shock–bubble interactions and the subsequent evolution of rotational flows. In addition, the FAST2D code, which incorporates FCT, has successfully handled problems containing both shocks and evolving subsonic rotational flows, like those generated by the shock–bubble interaction. One must anticipate that a shock-capturing algorithm would require a much finer grid for quantitative modelling of rotational flows involving material interfaces than for quantitative treatments of shocks alone. Thus a reasonably priced calculation with FCT will be useful primarily for studying the structural features of the shock–bubble interaction experiments. Fortunately this is our main objective. An additional concern in getting quantitatively correct calculations is the need to account for three-dimensional effects. Although three-dimensional FCT codes are available (FAST3D: Fyfe *et al.* 1985), the cost of running such calculations is unjustified, since our primary interest is in the physics of the problem and not in modelling specific experiments.

REFERENCES

Batchelor, G. K. 1967 *An Introduction to Fluid Dynamics*. Cambridge University Press.

Book, D. L., Boris, J. P., Kuhl, A. L., Oran, E. S., Picone, J. M. & Zalesak, S. T. 1981 Simulaion of complex shock reflections from wedges in inert and reactive gas mixtures. In *Proc. Seventh Int Conf. on Numerical Methods in Fluid Dynamics*, pp. 84–90.

Boris, J. P. 1976 Flux-corrected modules for solving generalized continuity equations. *Naval Research Laboratory Memo. Rep.* 3237.

Boris, J. P. & Book, D. L. 1976 Solution of continuity equations by the method of flux-corrected transport. *Methods in Computational Physics*, vol. 16, pp. 85–129. Academic.

Chern, I-L, Glimm, J., McBryan, O., Plohr, B. & Yaniv, S 1986 Front tracking for gas dynamics. *J. Comp. Phys.* **62**, 83–110.

Colella, P. & Woodward, P. R. 1984 The piecewise parabolic method (PPM) for gas-dynamical simulations. *J. Comp. Phys.* **54**, 174–201.

Didden, N. 1979 On the formation of vortex rings: rolling-up and production of circulation. *Z. Angew. Math. Phys.* **30**, 101–116.

Emery, M. H., Gardner, J. H., Boris, J. P. & Cooper, A. L. 1984 Vortex shedding due to laser ablation. *Phys. Fluids* **27**, 1338–1340.

Fritts, M. J. & Boris, J. P. 1979 The Lagrangian solution of transient problems in hydrodynamics using a triagular mesh. *J. Comp. Phys.* **31**, 173–215.

Fyfe, D. E., Gardner, J. H., Picone, J. M. & Fry, M. A. 1985 Fast three-dimensional flux-corrected transport code for highly resolved compressible flow calculations. In *Proc. Ninth Intl Conf. on Numerical Methods in Fluid Dynamics*. (ed. Soubbaramayer & J. P. Boujot), pp. 230–234. Springer.

Fyfe, D. E., Oran, E. S. & Fritts, M. J. 1989 Surface tension and viscosity with Lagrangian hydrodynamics on a triangular mesh. *J. Comp. Phys.* (to be published).

Gottlieb, D. 1985 Spectral methods for compressible flow problems. In *Proc. Ninth Intl Conf. on Numerical Methods in Fluid Dynamics* (ed. Soubbaramayer & J. P. Boujot), pp. 48–61. Springer.

Grinstein, F. F., Oran, E. S. & Boris, J. P. 1986 Numerical simulations of asymmetric mixing in planar shear flows. *J. Fluid Mech.* **165**, 201–220.

Haas, J.-F. L. 1983 Wave propagation and Rayleigh–Taylor instability in non-uniform gases. *Bull. Am. Phys. Soc.* **28**, 1359.

Hass, J.-F. L. 1984 Interaction of weak shock waves and discrete gas inhomogeneities. Ph.D. thesis, California Institute of Technology.

Haas, J.-F. L. & Sturtevant, B. 1987 Interaction of weak shock waves with cylindrical and spherical gas inhomogeneities. *J. Fluid Mech.* **181**, 41–76.

Harten, A. 1983 High resolution schemes for hyperbolic conservation laws. *J. Comp. Phys.* **49**, 357–393.

Lamb, H. 1945 *Hydrodynamics*, p. 202. Dover.

Landau, L. D. & Lifshitz, E. M. 1959 *Fluid Mechanics*, pp. 360–365. Pergamon.

Leonard, A. 1980 Vortex methods for flow simulation. *J. Comp. Phys.* **37**, 289–335.

Löhner, R. 1987 The efficient simulation of strongly unsteady flows by the finite element method. *AIAA*-87-055.

LÖHNER, R., MORGAN, K., PERAIRE, J. & VAHDATI, M. 1987 Finite element flux-corrected transport (FEM-FCT) for the Euler and Navier–Stokes equations. *Intl. J. Num. Meth. Fluids* **7**, 1093–1109.

LÖHNER, R., PICONE, M. & BORIS, J. P. 1988 Wave structure produced by shock propagation through single and multiple gas inhomogeneities. In *Proc. Sixteenth Intl Symp. on Shock Tubes and Waves*. VCH Verlagsgesellschaft (to be published).

MARKSTEIN, G. H. 1957*a* A shock tube study of flame front–pressure wave interactions. In *Sixth Symp. (Intl) on Combustion*, pp. 387–398. Reinhold.

MARKSTEIN, G. H. 1957*b* Flow disturbances induced near a slightly wavy contact surface, or flame front, traversed by a shock wave. *J. Aero. Sci.* **24**, 238.

MAXWORTHY, T. 1977 Some experimental studies of vortex rings. *J. Fluid Mech.* **81**, 465–495.

MESHKOV, Y. Y. 1970 Instability of a shock wave accelerated interface between two gases. *NASA TT F-13*, 074.

ORAN, E. S., YOUNG, T. R., BORIS, J. P., PICONE, J. M. & EDWARDS, D. H. 1983 A study of detonation structure: the formation of unreacted gas pockets. In *Nineteenth Symp. (Intl) on Combustion*, pp. 573–582. The Combustion Institute.

PICONE, J. M. & BORIS, J. P. 1983 Vorticity generation by asymmetric energy deposition in a gaseous medium. *Phys. Fluids* **26**, 365–382.

PICONE, J. M., BORIS, J. P., GREIG, J. R., RALEIGH, M. & FERNSLER, R. F. 1981 Convective cooling of lightning channels. *J. Atmos. Sci.* **38**, 2056–2062.

PICONE, J. M., ORAN, E. S., BORIS, J. P. & YOUNG, T. R. 1985 Theory of vorticity generation by shock wave and flame interactions. In *Dynamics of Shock Waves, Explosions, and Detonations*, pp. 429–448. American Institute of Aeronautics and Astronautics.

RICHTMYER, R. D. 1960 Taylor instability in shock acceleration of compressible fluids. *Commun. Pure Appl. Maths* **23**, 297–319.

RICHTMYER, R. D. & MORTON, K. W. 1967 *Difference Methods for Initial-Value Problems*, pp. 288–383. Wiley-Interscience.

RUDINGER, G. 1958 Shock wave and flame interactions. In *Combustion and Propulsion: Third AGARD Colloquium*, pp. 153–182. Pergamon.

RUDINGER, G. & SOMERS, L. 1960 Behaviour of small regions of different gases carried in accelerated gas flows. *J. Fluid Mech.* **7**, 161–176.

TAYLOR, G. I. 1953 Formation of a vortex ring by giving an impulse to a circular disk and then dissolving it away. *J. Appl. Phys.* **24**, 104.

WOODWARD, P. & COLELLA, P. 1984 The numerical simulation of two-dimensional fluid flow with strong shocks. *J. Comp. Phys.* **54**, 115–173.

YEE, H. C. 1987 Construction of explicit and implicit symmetric TVD schemes and their applications. *J. Comp. Phys.* **68**, 151–179.

ZALESAK, S. T. 1979 Fully multidimensional flux-corrected transport algorithms for fluids. *J. Comp. Phys.* **31**, 335–362.